Tailoring Cu Content in High-Entropy Alloys for Superior Bifunctional Electrocatalysis in Alkaline Water Splitting

Yuwen Pan, Guoning Ji, Boyao Zhang, Xin Li, Yongqi Tian, Shuangshuang Zhang, Depeng Zhao, Rongda Zhao, Fufa Wu, Lihua Miao

PII: S2352-4928(25)02462-6

DOI: https://doi.org/10.1016/j.mtcomm.2025.113950

Reference: MTCOMM113950

To appear in: *Materials Today Communications*

Received date: 6 August 2025
Revised date: 23 September 2025
Accepted date: 27 September 2025

Please cite this article as: Yuwen Pan, Guoning Ji, Boyao Zhang, Xin Li, Yongqi Tian, Shuangshuang Zhang, Depeng Zhao, Rongda Zhao, Fufa Wu and Lihua Miao, Tailoring Cu Content in High-Entropy Alloys for Superior Bifunctional Electrocatalysis in Alkaline Water Splitting, *Materials Today Communications,* (2025) doi:https://doi.org/10.1016/j.mtcomm.2025.113950

Tailoring Cu Content in High-Entropy Alloys for Superior Bifunctional Electrocatalysis in Alkaline Water Splitting

Yuwen Pan[a], Guoning Ji[a], Boyao Zhang[a], Xin Li[a], Yongqi Tian[a], Shuangshuang Zhang[a], Depeng Zhao[a], Rongda Zhao[a*], Fufa Wu[a,c]*, Lihua Miao[b*]

[a]School of Materials Science and Engineering, Liaoning University of Technology, Jinzhou, Liaoning 121000, P.R. China

[b]School of Medical Information Engineering, Shenyang Medical College, Shenyang, Liaoning, 110043, P. R. China

[c]Liaoning Technical University, Fuxin, 123000, P. R. China

Abstract

Electrocatalytic technology serves as a critical pathway for clean energy conversion, where high-entropy alloys demonstrate outstanding catalytic performance owing to their unique multi-principal-element design. This work systematically investigates $Cu_x(CoCrNiFe)_{100-x}$ HEAs as cost-effective bifunctional catalysts for both freshwater and seawater electrolysis. The optimized $Cu_{50}(CoCrNiFe)$ alloy exhibits excellent catalytic activity with low overpotentials of 248.3 mV for HER and 327 mV for OER at -10 mA cm^{-2} in alkaline freshwater, along with remarkable stability (<5% decay after 24 hours). Notably, in alkaline seawater electrolyte, it achieves even better HER performance (234 mV) while maintaining comparable OER activity, and demonstrates exceptional 50-hour durability in overall water splitting tests. These findings not only provide new insights into HEA-based catalyst design but also

highlight the great potential of such materials for practical large-scale hydrogen production from seawater resources, representing a significant step toward sustainable energy solutions.

Keywords: $Cu_x(CoCrNiFe)_{100-x}$; high entropy alloy; Overall water splitting; Hydrogen evolution reaction; Oxygen evolution reaction

Correspondences should be addressed: ffwu@lnut.edu.cn; Rongdazhaoln@126.com hellodepeng@163.com

1. Introduction

Facing the increasingly severe global energy crisis and environmental challenges, the development of efficient and sustainable energy conversion and storage technologies has become a crucial research direction in scientific studies [1-5]. Hydrogen energy serves as a pivotal secondary energy carrier bridging renewable energy sources and end-use applications, while water electrolysis for hydrogen production - with its advantages of zero carbon emissions, high purity, and flexible output adjustment - is regarded as one of the most promising technological pathways to achieve the "dual carbon" goals [6]. However, the inherent kinetic hysteresis of anodic oxygen evolution reaction (OER) and cathodic hydrogen evolution reaction (HER) and the contradiction between the reserve and cost of precious metal catalysts have become the core bottleneck restricting the large-scale application of electrolytic hydrogen production [7]. Compared with traditional alloys, HEAs are composed of five or more principal elements [8-10]. Through multi-element synergistic effect and lattice distortion effect, HEAs can significantly optimize the electronic structure, surface chemical state and stability of materials, thus providing rich catalytic active sites and

reducing reaction energy barriers [11]. It provides a new paradigm for the design of non-precious metal catalytic electrodes with high activity and long life, and becomes an ideal candidate material to replace precious metal catalysts.

Copper-based high-entropy alloys represent an emerging class of electrocatalysts demonstrating remarkable advantages through their distinctive physicochemical properties. While face-centered cubic (FCC) structured Cu-based HEAs exhibit exceptional mechanical toughness, corrosion resistance, and intrinsic activity in neutral-alkaline media, their practical current density remains constrained by insufficient active site exposure under high overpotentials and limited interfacial charge transfer efficiency [12]. Copper possesses exceptional electrical conductivity and cost-effectiveness. When incorporated in optimal amounts, Cu can simultaneously modulate the alloy's electronic structure to reduce hydrogen adsorption free energy while inducing localized charge redistribution through electronegativity differences with the host matrix. This dual functionality renders Cu-modified alloys particularly promising for enhancing both the HER and OER intrinsic activities [13-14]. It can be seen from the performance data summarized in Table 1 that the Cu-containing electrocatalyst exhibits a wide range of activity for hydrogen evolution reaction and oxygen evolution reaction in alkaline electrolyte. Copper-based high-entropy alloys can show great potential in the field of electrocatalysis through multi-component design and synergy, providing a new direction for the design and development of efficient catalysts. In recent years, Cu-doped high-entropy alloys have shown great potential as electrocatalysts for water splitting. These studies usually focus on the electronic structure regulation and multiple synergistic effects caused by the introduction of Cu element to enhance the adsorption energy of the reaction intermediates [23]. However, most of the reported copper-containing high-entropy alloys aim to form a single-phase

solid solution, or only focus on the catalytic performance after amorphization and nanocrystallization. There is still a lack of systematic research on the macroscopic phase separation behavior driven by thermodynamics during solidification and its unique contribution to catalytic performance.

Different from the above work, a stable two-phase structure composed of Cu-rich phase (FCC1) and CoCrNiFe-rich phase (FCC2) was intentionally constructed by using the positive mixing enthalpy between Cu and other elements in the Cu_x $(CoCrNiFe)_{100-x}$ system studied in this paper. This unique phase separation structure not only provides abundant phase interfaces, induces strong lattice distortion and electron coupling effects, but also forms multiple synergistic sites with different compositions and coordination environments. By accurately adjusting the copper content (x value) in the alloy, the electrocatalytic performance is deeply optimized, which endows it with extremely high application value in the field of electrocatalysis. The multi-component characteristics of the alloy have created a complex and changeable chemical environment on its surface, which has spawned a large number of active sites and significantly improved the electrocatalytic activity. In 1 M KOH electrolyte, Cu_{50}(CoCrNiFe) alloy exhibits excellent HER and OER performance: when the current density is 10 mA cm^{-2}, the HER overpotential is only 248.3 mV, the OER overpotential is 327 mV, and the Tafel slope is excellent. After 24 hours of cycle test, the performance attenuation is less than 5 %, and the stability is extremely strong. This study was further extended to the alkaline seawater electrolysis environment to test the HER and OER properties of $Cu_x(CoCrNiFe)_{100-x}$ alloy. At a current density of 10 mA cm^{-2}, the HER overpotential of Cu_{50}(CoCrNiFe) alloy is as low as 234 mV, and the OER overpotential is maintained at 327 mV. After 24 h cycle test, the stability is still excellent. In alkaline seawater electrolysis environment, the electrocatalytic performance of the alloy is better than that

under traditional alkaline conditions. On the contrary, its unique ionic composition provides better catalytic conditions for copper-based high-entropy alloys, making them exhibit higher performance in alkaline seawater electrolysis. This study aims to clarify the key role of this specific dual FCC phase microstructure in regulating the catalytic activity and stability of electrolytic water (especially seawater electrolysis), and provides a new perspective for the design of high-entropy alloy catalysts.

2. Experimental methods

2.1 Materials

High purity copper particles, high purity cobalt particles, high purity chromium particles, high purity nickel particles, high purity iron particles. Potassium hydroxide (KOH, AR, Aladdin Inc.), natural seawater (collected off the coast of Huludao, China).

2.2 Preparation of bulk electrode

In the pretreatment stage, the surface oxide skin of all metal raw materials is removed by grinding wheel until the uniform bright surface is exposed. Subsequently, it was immediately transferred to an analytical balance with an accuracy of 0.1 mg for quality determination. In order to prevent the oxidation of well-weighed metal raw materials from affecting the properties of the alloy, the metal raw materials were sealed in a vacuum sample bag after weighing. According to the design composition of $Cu_x(CoCrNiFe)_{100-x}$ (x = 50,60,70,80 at %), the ingots were referred to as Cu50, Cu60, Cu70 and Cu80. The DXL-500II non-consumable tungsten vacuum arc furnace was used for smelting: the cavity was pre-vacuumized at 5×10^{-3} Pa and filled with high-purity Ar (99.999 %) to 0.05 M Pa. The Ti ingot was first smelted for 2 min to capture residual oxygen. The smelting process was repeated for 4 times, 3-5 min each time, and magnetic stirring was performed once (30s) to ensure uniform chemical composition.

The alkaline seawater electrolyte used in this study was prepared by dissolving

potassium hydroxide in natural seawater, stirring violently until it was completely dissolved. After centrifugation at 6000 rpm for 10 minutes to remove most of the organisms and suspended particles, the final concentration of seawater KOH was 1 mol L^{-1}.

2.3 Material characterization test

The D/max-2500 X-ray diffractometer with Cu Kα ray source (λ = 1.5406 Å) was used to analyze the phase and chemical state. The working parameters were set as follows: tube pressure 40 kV, tube current 100 mA, scanning range 20-100°, scanning rate 8° min^{-1}; the elemental composition and valence information were studied by X-ray photoelectron spectroscopy (XPS, ESCALAB250). The surface morphology and structural characteristics were observed by high resolution imaging using Zeiss-Sigma 500 field emission scanning electron microscope.

2.4 Electrochemical test

All electrochemical tests were performed on the CHI760E electrochemical workstation (Chenhua Instrument). The electrochemical performance was tested by a standard three-electrode system in 1 M KOH (pH = 13.7) and 1 M KOH solution (pH = 13.51) of seawater. A ball bump electrochemical sample with a gauge size of 5 mm × 5 mm × 2 mm (thickness) was cut from the melted sample by wire cutting EDM method. The surface of the cut sample was polished to a smooth mirror as the working electrode, and the surface oxides and impurities were removed. The geometric area of the working part is 0.25 cm^2. All the performance calculations about the area are based on the geometric area of the working electrode. Hg/HgO was used as the reference electrode, and Pt electrode/carbon rod was used as the counter electrode for OER/HER test. Linear sweep voltammetry (LSV), cyclic voltammetry (CV), electrochemical impedance spectroscopy (EIS) and cyclic stability test (it) were obtained. The iR compensation is

performed before the linear sweep voltammetry (LSV) test. The open circuit potential test is performed first, and the value is recorded after the potential is stabilized. In the iR compensation setting, the compensation degree is set to 90% to effectively eliminate the influence of most of the solution resistance, while avoiding curve distortion caused by overcompensation. The voltage of HER and OER is converted into a value related to RHE using the following formula: E (vs. RHE) = $E_{(vs.\ Hg\ /\ HgO)}$ + 0.059 * pH + 0.098 V. When drawing the C_{dl} diagram, the non-faradaic interval is first determined, and CV tests are performed at a series of different scanning rates (10,20,30,40,50 mV s^{-1}) in this interval. At a fixed potential, the average value of the anode scanning current and the cathode scanning current [24] is taken to obtain the relationship between Δj and the scanning rate, and the slope is the electric double layer capacitance, namely C_{dl}. In addition, the electrochemical OER/HER stability was tested by chronopotentiometry at 50 mA cm^{-2} for 24 h. The overall water splitting performance test uses a two-electrode system with a corresponding scan rate of 5 mV s^{-1}.

3. Results and discussion

3.1 Crystal structure and microstructure analysis

In order to explore the factors affecting the performance of water electrolysis, the structure was characterized. Fig.1a is the XRD pattern of as-cast $Cu_x(CoCrNiFe)_{100-x}$ (x = 50,60,70,80) alloys. It can be observed that the alloy is composed of double FCC phases, that is, the liquid phase separation occurs during the solidification process of the alloy. Due to the low melting point of Cu and its incompatibility with CoCrNiFe, Cu element segregation occurs, resulting in liquid phase separation. In the process of solidification or heat treatment, Cu is easy to segregate to the grain boundary or interdendritic region, forming a copper-rich phase. The copper-rich phase forms an

interface with adjacent elements such as Ni, Fe, and Co, produces an electronic coupling effect, optimizes the center position of the d-band, enhances the adsorption / desorption ability of the reaction intermediate, and provides multiple synergistic sites [25]. The lattice distortion of the copper-rich phase can also induce the formation of ladders, defects, or twin boundaries on the surface. These low-coordinated atoms usually have higher intrinsic catalytic activity. With the increase of Cu content, the phase composition of the alloy did not change, but the diffraction intensity of the FCC_1 phase gradually increased, and the diffraction intensity of the FCC_2 phase gradually decreased. And the main diffraction peak shifted with the increase of Cu content. In order to quantify the change of phase composition with Cu content, the peak area of FCC1 and FCC2 phases in the XRD pattern was compared (An inset in Fig.1a). The results show that with the increase of Cu content from 50% to 80%, the relative content of FCC1 phase (Cu-rich phase) increases from 65.8% to 78.3%, while that of FCC2 phase (CoCrNiFe phase) decreases from 34.2% to 21.7%. The grain size of FCC1 phase increases with the increase of Cu content, indicating that the dendritic structure gradually decreases and the alloy tends to have a more uniform phase distribution.

The decrease of dendritic structure usually means a more uniform microstructure, but in this study, the higher Cu content leads to an increase in the proportion of Cu-rich phase (FCC1) and a decrease in the proportion of CoCrNiFe-rich phase (FCC2). Since the FCC2 phase contains more elements with high intrinsic catalytic activity (such as Ni, Fe, Co), its reduction directly leads to a decrease in the number of active sites. In addition, although the Cu-rich phase can optimize the electronic structure through the

interface effect, its own adsorption capacity for the hydrolytic intermediate is weak, which is not enough to compensate for the loss of activity caused by the reduction of FCC2 phase. Therefore, although the dendritic fraction decreases, the overall catalytic activity still decreases with the increase of Cu content. In the design of high-entropy alloys, the influence of phase composition and relative content on the catalytic performance is much higher than the contribution of dendrite morphology. It is worth noting that unlike most single-phase CuCoCrNiFe high-entropy alloys reported in the literature [26-27], the alloys in this work exhibit a clear dual FCC phase structure. This structure originates from the thermodynamically driven liquid phase separation, rather than the traditional single-phase solid solution formation mechanism. This provides an ideal platform for studying the influence of phase interface and composition fluctuation on catalytic performance.

Fig.1b is the microstructure of as-cast $Cu_x(CoCrNiFe)_{100-x}$ (x = 50,60,70,80) alloys. When the Cu content is 50 %, the Cu50 alloy is composed of dendrites and interdendritic structures. When the Cu content is more than 50 %, Cu60, Cu70 and Cu80 alloys are composed of dendrites and interdendritic structures, but the dendrite morphology changes from dendrites to circular structures, and some precipitates are precipitated in the interdendritic region, as shown in the figure. The dendrite content in the alloy was analyzed. When the Cu content was 50 %, the dendrite integral number of Cu50 alloy was 46.24 %. With the increase of Cu content, the volume fraction of dendrites decreases gradually. When the Cu content is 60 %, the number of dendrites is 33.39 %. When the Cu content is further increased to 70 % and 80 %, the branch crystal

integrals are reduced to 25.49 % and 12.57 %, respectively. Fig.1c is the surface scanning distribution map of Cu50 alloy. It can be seen from the figure that Fe, Co, Cr and Ni elements are evenly distributed on the dendrites, and the color of the metal Cu is clearly distinguished from other colors and is mainly distributed between the dendrites.

3.2 Chemical state analysis

In order to verify the chemical state and electronic structure, X-ray photoelectron spectroscopy was performed on the Cu50 alloy before and after the stability test. Fig.2a is the total XPS spectrum of the surface of $Cu_x(CoCrNiFe)_{100-x}$ high-entropy alloy. The experimental results show that each element (Co/Cr/Cu/Fe/Ni) is a spin-orbit splitting bimodal structure, that is, $2p_{3/2}$ and $2p_{1/2}$ [24]. Fig.2b shows the Co 2pXPS spectrum of the Cu50 sample. The overall spectrum shape is in the range of 810-775 eV, and the characteristic peak of Co^0 $2p_{3/2}$ is shown at the binding energy of about 778.8 eV, indicating that the metal state of Co exists in the sample, indicating that some unoxidized metal Co is exposed in the alloy matrix, which is consistent with the slight oxidation behavior of the HEA surface. In addition, Co also exists in the form of oxide in the sample. The main peak of $2p_{3/2}$ is located at the binding energy of 781.28 eV, corresponding to the energy levels of Co^{3+} $2p_{3/2}$ and Co^{2+} $2p_{3/2}$. The main peak of $2p_{1/2}$ is located at the binding energy of 796.78 eV, corresponding to the energy levels of Co^{3+} $2p_{1/2}$ and Co^{2+} $2p_{1/2}$. The distance ΔE between the two is about 15.5 eV, which is consistent with the reference energy difference between Co and its oxidation state. Obvious satellite peaks (Sat.) can be observed on both sides of the main peak. These

peaks are caused by energy loss or other electronic structure effects during electron transition, which appear at 787.18 eV and 802.28 eV, respectively. The relative intensity is about 30-40 % of the corresponding main peak. Fig.2c shows the Cr 2p XPS spectrum of Cu50 sample, showing the characteristic peak of Cr^0 at the binding energy of about 573.14 eV, and the area ratio of trace Cr^0 is less than 10 %, indicating that there is a small amount of unoxidized metal Cr on the surface of the alloy. At 576.35 eV and 586.30 eV, Cr^{3+} $2p_{3/2}$ and Cr^{3+} $2p_{1/2}$, Cr^{2+} $2p_{1/2}$ oxidation state characteristic peaks were shown respectively. The spectrum shows that Cr mainly exists in the form of Cr^{3+}, forming a dense passivation film. Fig.2d shows the Cu 2p XPS spectrum. The main peak of $2p_{3/2}$ is located at 932.76 eV, and the main peak of $2p_{1/2}$ is located at 952.91 eV, indicating that Cu mainly exists in the metal state in the alloy. The XPS spectrum of Fe 2p is shown in Fig.2e. The spectrum shows that the metallic iron and iron oxide coexist in the alloy. The main peak of metallic Fe^0 $2p_{3/2}$ is located at 707.21 eV, and the full width at half maximum is narrow, which corresponds to the metallic iron in the alloy. Fe^{2+} $2p_{3/2}$ is 711.99 eV, Fe^{3+} $2p_{3/2}$ is 714.69 eV, Fe^{2+} $2p_{1/2}$ is 722.95 eV, Fe^{3+} $2p_{1/2}$ is 725.51 eV. The proportion of Fe^{2+} and Fe^{3+} is significant, indicating that divalent iron and trivalent iron oxides are the main surface phases. Two satellite peaks can be observed at 719.66 eV and 729.82 eV. Fig.2f shows the Ni 2p XPS spectrum of Cu50 sample. The Ni 2p spectrum shows the Ni^0 metallic state at 852.60 eV (Ni^0 $2p_{3/2}$) and 869.98 eV (Ni^0 $2p_{1/2}$), and the peak shape is narrow and symmetrical, corresponding to the metal Ni in the alloy. The peaks at 855.86 eV and 873.79 eV correspond to Ni^{2+} $2p_{3/2}$ and Ni^{2+} $2p_{1/2}$, and the broad peaks at 861.48 eV and 879.41 eV correspond to the

satellite peaks of Ni $2p_{3/2}$ and Ni $2p_{1/2}$, indicating that there is a NiO-based oxide layer on the surface of the sample, and a large amount of metallic Ni^0 is still exposed in the alloy matrix.

The presence of both metallic and oxidized states on the alloy surface can ensure good electronic conductivity, reduce charge transfer resistance, and optimize the adsorption-desorption free energy of *OH / *OOH intermediates, thereby improving OER activity. In addition, the dense Cr_2O_3 passivation layer formed by Cr^{3+} constructs a stable oxide film on the surface, which effectively inhibits Cl erosion and significantly improves the long-term stability in seawater electrolysis. Therefore, the synergistic electronic structure regulation and surface passivation effect of metal-oxide state can jointly determine the high activity and durability of high-entropy alloys in freshwater and seawater.

3.3 Electrochemical properties of materials

Fig.3 shows the HER performance of Cu50-Cu80 samples in 1.0 M KOH alkaline electrolyte. It can be seen from Fig.3a that compared with Cu60 (271.8 mV @ -10 mA cm^{-2}), Cu70 (280.7 mV @ -10 mA cm^{-2}) and Cu80 (303.4 mV @ -10 mA cm^{-2}) samples, Cu50 alloy (248.3 mV @ -10 mA cm^{-2}) has a lower overpotential, indicating that Cu50 alloy has the highest intrinsic catalytic activity. The corresponding Tafel slope obtained by LSV curve is shown in Fig.3b.Among all the contrast samples, the Tafel slope of Cu50 alloy (151.33 mV dec^{-1}) is the lowest, which is lower than that of Cu60 (153.46 mV dec^{-1}), Cu70 (156.96 mV dec^{-1}) and Cu80 (168.59 mV dec^{-1}) samples, indicating that the HER kinetic barrier is the lowest, the electrocatalytic reaction rate is the most

sensitive to the change of overpotential, and the electron transfer kinetics is more rapid. It can be seen from Fig.3c that when the current density is -10 mA cm^{-2}, the overpotential of the alloy sample increases monotonously with the increase of Cu content, and the overpotential of the Cu50 sample is the lowest. The Cu50 alloy exhibits the best HER activity, which may be attributed to its optimal dual-phase ratio and maximum phase interface density. In Cu50, FCC2 phase (rich in highly active Ni, Co, Fe) and FCC1 phase (rich in Cu) form a continuous and interpenetrated network structure, which maximizes the exposure of rich phase interfaces [28]. The lattice distortion and electron coupling effects at these interfaces optimize the d-band center, thereby optimizing the hydrogen adsorption free energy (ΔG_H*). In contrast, higher Cu content (such as Cu80) leads to a sharp decrease in FCC2 phase. Although the dendrite structure is more uniform, the number of valuable high active sites is significantly reduced, which reduces the catalytic activity. Electrochemical impedance spectroscopy (EIS) also plays an important role in catalyst kinetics. Fig.3d shows the HER electrochemical impedance spectroscopy of Cu50-Cu80 alloy. In the high frequency region, the semicircle diameters of the four samples are not much different, and all have smaller semicircle diameters, which is closely related to the charge transfer rate on the electrode surface. The smaller the diameter, the lower the charge transfer impedance and the faster the electrochemical reaction kinetics. In the low frequency region, the slope of Cu80 alloy is the largest, which is higher than that of other samples, and the diffusion rate is faster. The Cu50 alloy with higher HER activity was subjected to multi-impedance test. Fig.3e is the Bode diagram of Cu50 alloy, which shows the

phase angle-frequency curve of the kinetic characteristics of the reaction catalyst. Various voltages corresponding to -5 mA cm^{-2}, -10 mA cm^{-2}, -20 mA cm^{-2} to -100 mA cm^{-2}. With the increase of the applied potential, the phase angle in the low frequency region gradually decreases, the charge transfer resistance continues to decrease, and the charge transfer rate increases. It shows that there is a mixed control of charge transfer and diffusion in the system [29]. It can be seen that the catalyst has a fast electron transfer rate and good catalytic performance. Fig.3f is the relaxation time distribution (DRT) of the Cu50 sample, which further explains the polarization impedance. The transverse axis is the relaxation time τ, showing the reaction speed of each electrochemical step [30-31]. The longitudinal axis is γ (τ), indicating the amount of charge or resistance contributed on this time scale. The DRT diagram shows that as the logarithm of relaxation time increases, the main peak value increases first and then decreases, and the peak position is short and the amplitude is high, indicating that the charge transfer process is fast and the interface capacitance is small. It shows that the charge transfer resistance and polarization impedance of the electrode interface are reduced, thus accelerating the charge transfer process. In order to investigate the activity of the catalyst, the electrochemical surface area (ECSA) is an important parameter of electrocatalytic performance [32]. We estimated it by measuring the electric double layer capacitance (C_{dl}). It can be seen from Fig.3g that the Cu80 alloy has the highest C_{dl} value (0.00415 mF cm^{-2}), while the Cu50 alloy with the best HER performance exhibits the lowest C_{dl} value (0.00216 mF cm^{-2}). The negative correlation between the C_{dl} value and the catalytic activity indicates that the HER performance of the catalyst

is not mainly determined by the number of active sites, but by the intrinsic activity of the active sites. The lower C_{dl} value of Cu50 alloy may be due to its unique surface electronic structure. This may be due to the stronger electronic interaction induced by the composition optimization of Cu50 alloy, which significantly improves the intrinsic catalytic efficiency of each active site. This means that although the physical surface area or capacitive area exposed by the Cu50 alloy is relatively small, each of its active sites has a much higher ability to drive the hydrogen evolution reaction than other samples. Therefore, Cu50 alloy achieves higher conversion frequency and excellent overall performance. Subsequently, the Cu50 alloy electrocatalyst with the best catalytic activity was subjected to a 24-hour cycle test at a current density of -50 mA cm^{-2}. The cycle stability is one of the important indicators to measure the catalytic performance of the sample. We evaluated the long-term reliability of the catalyst by chronopotentiometry. As shown in Figure 3h (the illustration in the figure is the LSV curve before and after the cycle), the Cu50 sample not only exhibits very excellent cycle stability after 24 h of cycle, but also the LSV curve after the cycle has been improved.

The OER performance of the samples in 1.0 M KOH alkaline electrolyte was studied. It can be seen from Fig.4a that at a current density of 10 mA cm^{-2}, the OER overpotential of Cu50 is 327 mV, the overpotential of Cu60 is 317.9 mV, and the overpotentials of Cu70 and Cu80 alloys are 327.7 mV and 332 mV, respectively. Cu60 alloy has the lowest overpotential, but it is not much different from other samples. Fig.4b shows the corresponding Tafel slope. Cu60 alloy still has the lowest Tafel slope of 57.6 mV dec^{-1}, which is lower than that of Cu50 (61.95 mV dec^{-1}), Cu70 (61.21 mV

dec^{-1}) and Cu80 (62.4 mV dec^{-1}) alloys. Fig.4c shows the overpotential of Cu50-Cu80 alloy at the current density of 10 mA cm^{-2},50 mA cm^{-2} and 100 mA cm^{-2}, which is consistent with the change trend of LSV and Tafel slope. Fig.4d is the OER electrochemical impedance spectroscopy of the alloy. In the high frequency region, both Cu50 and Cu80 alloys have a small semicircle diameter. Rct directly affects the speed of OER kinetics. The smaller the charge transfer resistance, the faster the charge transfer, and the higher the OER activity. It can be seen that Cu50 and Cu80 alloys have higher activity. Similarly, the Cu50 alloy was tested for multiple impedances. The Bode diagram of the Cu50 alloy is shown in Fig.4e. It can be seen that as the applied potential increases, the phase angle in the intermediate frequency region continues to decrease, Rct continues to decrease, and the charge transfer rate continues to increase. The process of mass transfer to the electrode surface is relatively rapid and efficient, and has high activity. Fig.4f is the DRT spectrum of Cu50 alloy. The high entropy effect in the alloy synergistically reduces the *OH desorption energy barrier through the three paths of 'defect freezing - d band broadening - charge delocalization'. The hysteresis diffusion preserves the vacancies and step defects generated during the polarization process and becomes a highly exposed *OH geometric active site. The lattice distortion caused by multi-principal elements shifts the d-band center down and weakens the M-O bond strength. The proton-electron coupling channel provided by the M-O boundary reduces the activation energy of the Heyrovsky step, and the desorption energy barrier decreases. At the same time, the valence electron delocalization significantly reduces the interface capacitance and the charge rearrangement. The combined effect of the

three is that the τ_2 (Rct) in the DRT spectrum decreases monotonically with the negative shift of the potential and the peak area continues to shrink, accelerating the charge transfer [33]. In order to further explain the reasons affecting OER activity, Fig.4g shows the C_{dl} value of the synthesized sample. Cu50 and Cu60 have high C_{dl} values, which are 0.01119 mF cm^{-2} and 0.01151 mF cm^{-2}, respectively, indicating that the surface of Cu50 and Cu60 alloys has a large active area and high catalytic activity. In 1.0 M KOH, Cu60 alloy exhibits the best OER intrinsic activity, but from the overall performance of the total hydrolysis application, the OER activity of Cu50 is not much different from it, and it has more potential. First of all, Cu50 exhibits excellent bifunctionality, and it also has the lowest overpotential and Tafel slope in HER (Fig.3), which is the best performance in the same series. This means that Cu50 can be used as the same electrode material for both cathode and anode, greatly simplifying the design of the full hydrolysis device and reducing costs. Although the OER activity of Cu60 is slightly higher, its HER performance is not as good as that of Cu50, resulting in its overall hydrolysis performance lagging behind. Secondly, Cu50 exhibits a lower charge transfer resistance in the OER process, indicating that it has excellent electron transport capacity, which is beneficial to the efficient reaction at high current density. Therefore, Cu50 achieves the best balance between HER and OER activity, conductivity and stability, and is the only component in this series that achieves top performance in both types of reactions, which has more practical application value. Based on the above advantages, we further tested the cycle stability of Cu50 alloy. Fig.4h shows that the current is almost not attenuated after 24-h of reaction at room temperature at a current

density of 50 mA cm^{-2}, showing excellent cycle stability. The illustration in the figure is the LSV curve before and after the cycle stability test, the SEM diagram and the EDS diagram after the test. It can be seen that after the stability test, the catalyst exhibits further improvement in performance, and the mechanism can be attributed to the common results of surface reconstruction and element synergy. The EDS elemental distribution analysis shows that Fe, Co, Cr and Ni elements maintain a highly uniform and overlapping distribution on the micron scale, indicating that the main structure of the high-entropy alloy has excellent stability under harsh electrochemical conditions, and no obvious phase separation or element segregation occurs, providing a stable and rich active site for the catalytic reaction. At the same time, the Cu element was partially selectively dissolved during the test process, inducing the formation of worm-like corrosion pits and fluffy structures on the surface of the catalyst, which significantly increased the electrochemical active area. More importantly, during the repeated polarization process, Co^{2+}, Fe^{2+} and Ni^{2+} in the surface layer were continuously oxidized to highly active CoOOH, FeOOH and NiOOH (XPS results confirmed that the proportion of high valence states increased significantly). These in-situ generated high-valent hydroxyl oxides not only have better hydrogen adsorption free energy (ΔG_H), but also optimize the OH ↔ *OOH conversion energy barrier and significantly accelerate the hydrogen evolution reaction kinetics. On the other hand, the 'hysteresis diffusion effect' unique to the high-entropy matrix effectively inhibits the continuous loss of Cu elements and accurately limits the thickness of the surface reconstruction layer to the range of 1-3 nm. The structure maintains the integrity of the

overall structure while fully exposing the highly active sites and avoids performance degradation caused by excessive corrosion.

In summary, the excellent bulk phase stability of high-entropy alloys and Cu-induced dynamic surface reconstruction achieve a synergistic unity: the main structure provides a stable carrier for the catalytic reaction, and the confined surface reconstruction layer significantly enhances the intrinsic activity, both of which jointly promote the catalyst to maintain long-term stability while achieving further enhancement of activity.

In order to evaluate the effect of the cycle test on the surface chemical state of the catalyst, the samples after the cycle test were also characterized by XPS. Fig.5a shows the XPS full spectrum of Cu50 alloy after cycling. Compared with the initial spectrum, the characteristic peaks of the main elements did not shift significantly, indicating that the crystal skeleton remained intact. Fig.5b is the Co 2p spectrum before and after the cycle. Before and after the cycle test, the peak position and intensity of the Co $2p_{3/2}$ orbital and $2p_{1/2}$ orbital do not change much. After the cycle, the Co^0 signal appears in the $2p_{1/2}$ spectrum, which is not derived from the ' new ' metal Co. It is a long-term electrochemical polarization that promotes the continuous dissolution / redeposition of the outermost high-valence CoOOH, accompanied by an increase in surface roughness. When the roughness scale is comparable to the photoelectron inelastic mean free path, the subsurface Co^0, which is completely covered by the oxide layer, begins to contribute to the signal, resulting in a Co^0 peak at $2p_{1/2}$ near 793.3 eV. The Cr 2p spectrum of Fig.5c shows that Cr^{2+} $2p_{3/2}$ is completely oxidized to Cr^{3+} $2p_{3/2}$ after the cycle, and

Cr^{2+} $2p_{1/2}$ is almost completely oxidized to Cr^{3+} $2p_{1/2}$ after the cycle, and the peak intensity is slightly reduced. After the cycle, Cr is enriched in the dense passivation layer in the form of Cr^{3+} and a small amount of Cr^{2+}, which can maintain high conductivity through interfacial charge rearrangement [34]. It is a key chemical barrier for the long-term stable operation of Cu-based high-entropy alloys. The Cu 2p spectrum is shown in Fig.5d.After the cycle, it still exists in the metal state, and the peak position is almost not shifted, and the peak intensity does not change significantly, which provides a key chemical basis for Cu-based alloys to maintain electrochemical activity and stability under long-term alkaline conditions. Fig.5e is the Fe 2p spectrum before and after the cycle. The main peak of $2p_{3/2}$ moves to 712.44 eV as a whole, and the satellite peak (719.84 eV) intensity increases. The spectrum shows that the proportion of Fe^{3+} $2p_{3/2}$ increases significantly, while the peak intensity of $2p_{1/2}$ decreases as a whole. After the cycle, Fe exists in the form of a dense oxide layer dominated by Fe^{3+}, which can provide rich OER active sites, and cooperate with the Cr_2O_3 passivation layer to inhibit corrosion. The Ni 2p spectrum of Fig.5f shows that Ni^{2+} $2p_{3/2}$ and Ni^{2+} $2p_{1/2}$ are partially oxidized to Ni^{3+} $2p_{3/2}$ and Ni^{3+} $2p_{1/2}$, the intensity of the main peak does not change much, and the intensity of the two satellite peaks decreases. After the cycle test, most of the elements are oxidized to an oxidation state with more catalytic activity, which significantly improves the intrinsic activity of electrocatalytic, and inhibits corrosion through a dense oxide film to achieve synergistic optimization of activity-stability. This transition to a higher valence state is crucial to enhance the intrinsic catalytic activity. DFT calculations and related literature show that [35-36], the

hydroxyl oxides (such as NiOOH, FeOOH, CoOOH) formed by the oxidation of Ni/Fe/Co elements are the real active species of OER. Among them, Ni^{3+}/Ni^{4+} is the key center of charge transfer in the OER process, which can significantly reduce the energy barrier of O-O coupling. At the same time, the incorporation of Fe^{3+} can regulate the electronic structure of the Ni/Co site and optimize the adsorption free energy of the oxygen intermediates (*O, *OH, *OOH), making it closer to the vertex of the volcanic map. The presence of Co^{3+} is helpful to stabilize the high-valent Ni species and promote its formation. In this work, the surface reconstruction layer rich in highly active Ni (Fe/Co) OOH is formed by the transformation of $Ni^{2+}\rightarrow Ni^{3+}$,$Fe^{2+}\rightarrow Fe^{3+}$ and $Co^{2+}\rightarrow Co^{3+}$ after cycling. This 'in-situ surface activation' process exposes a large number of highly active sites, which explains the phenomenon that the LSV performance is improved after the cycle.

The $Cu_x(CoCrNiFe)_{100-x}$ high-entropy alloy electrolytic water has excellent catalytic performance and stability in alkaline electrolytic environment. However, the shortage of freshwater resources has become a bottleneck restricting the large-scale production of green hydrogen. In contrast, a large number of seawater resources on the earth provide almost unlimited hydrogen sources. However, seawater is rich in corrosive ions such as Cl, which can easily lead to side reactions (such as chlorine evolution reaction, ClER) and catalyst deactivation. The Cu-based high-entropy alloy can form a self-healing active layer in alkaline seawater due to the multi-principal element hysteresis diffusion and the natural inertness of Cu to Cl^-, which not only inhibits chlorine corrosion but also continues to regenerate the active sites [37]. At the

same time, the synergistic effect between Cu and Fe/Co/Ni optimizes the coupling of HER-H adsorption and OER-O, achieving high catalytic activity, high selectivity and long durability, providing an efficient bifunctional catalytic scheme for large-scale green hydrogen production of seawater instead of fresh water.

Next, the electrochemical test of $Cu_x(CoCrNiFe)_{100-x}$ high entropy alloy was carried out in alkaline seawater electrolyte with pH 13.51. Firstly, Fig.6a shows the LSV curve of Cu50-Cu80 alloy HER. The HER catalytic activity of Cu50 alloy is still higher than that of other samples. At the current density of -10 mA cm^{-2}, the overpotential is 234 mV, which is lower than that in alkaline electrolyte. The catalytic activity of Cu60 (242 mV @ -10 mA cm^{-2}), Cu70 (280 mV @ -10 mA cm^{-2}) and Cu80 (246 mV @ -10 mA cm^{-2}) samples is also higher than that in alkaline electrolyte. It may be due to the fact that in alkaline seawater, Cu, Cr, Ni and other elements do not form their own independent film, but form a multi-layer coupled and dynamically repairable passivation network under the chemical ' stimulation ' of Cl , thus achieving corrosion resistance and active site exposure at the same time. Cr^{3+} forms a dense Cr_2O_3 barrier in the outermost layer, and Ni^{2+}/Cu^{2+} forms a $Ni(OH)_2$ / $Cu(OH)_2$ layered film in the outermost layer, which can exchange Cl^- between layers and re-deposit in situ to repair defects. Fe^{2+} is oxidized to γ-FeOOH in the innermost layer, providing a rigid skeleton and electronic channel to realize the sandwich structure of 'outer dense-inner active-self-healing' [38-39]. Each layer of elements achieves synergistic passivation through ion exchange, charge coupling and dynamic redeposition. It not only blocks Cl pitting, but also ensures the continuous exposure of NiOOH/CoOOH active sites. This makes

Cu-based HEA not only resistant to corrosion but also maintain high activity in seawater. However, in the absence of Cl 's ' stimulus ' in soda solution, the passivation film may not be dense enough, which reduces the exposure of active sites. The Tafel slope of Fig.6b also shows that Cu50 (119.4 mV dec^{-1}) has the lowest Tafel slope, and the Tafel slope of all samples in alkaline seawater electrolyte is lower than that in alkaline electrolyte. Fig.6c is the corresponding overpotential histogram of Cu50-Cu80 alloy at a current density of -10 mA cm^{-2}. Fig.6d is the HER electrochemical impedance spectroscopy of the alloy, all of which show typical single capacitive arc characteristics, and there is no obvious diffusion tail in the high frequency region, indicating that it is mainly controlled by the charge transfer process and has low ion diffusion resistance [40]. The Cu50 alloy with the lowest overpotential was also tested by multi-impedance. The Bode diagram of Cu50 alloy is shown in Fig.6e. The diagram shows that the system has obvious charge transfer impedance but no significant film layer, and the phase angle has a single wide peak. The overall behavior is consistent with the Nyquist diagram, showing a uniform corrosion process controlled by charge transfer, and the charge transfer rate is increasing. The DRT spectrum of Cu50 alloy is shown in Fig.6f, which shows a significant and sharp main peak, indicating that there is only one dominant electrochemical process in the system, that is, charge transfer reaction, no additional low-frequency peaks, excluding the influence of passivation film or diffusion process [41], which is consistent with the results of Nyquist diagram and Bode diagram. The C_{dl} values of Cu50 (0.00279 mF cm^{-2}), Cu60 (0.00269 mF cm^{-2}), Cu70 (0.00281 mF cm^{-2}) and Cu80 (0.00277 mF cm^{-2}) alloys in Fig.6g are not much different, all of which

have multiple active sites and excellent catalytic activity. It can be seen that the Cu50 sample exhibits excellent electrocatalytic performance in the alkaline seawater electrolysis environment, and the cycle stability of Cu50 is tested. It can be seen from Fig.6h that after 24h of testing, the alloy has very excellent stability, and the LSV curve after cycling is better. This is attributed to the selective dissolution-redeposition process on the surface under the synergistic effect of Cl, the density of active sites and the intrinsic activity are simultaneously increased [42], and the catalytic performance is enhanced. In addition, the dense Cr_2O_3 passivation layer formed by Cr^{3+} also effectively inhibits Cl corrosion, which significantly improves the long-term stability in seawater electrolysis. In addition, the excellent corrosion resistance and stability of the alloy in alkaline seawater may also be due to its unique dual-phase structure. The Cu-rich phase (FCC1) has a natural inertness to Cl, while the CoCrNiFe-rich phase (FCC2) provides high catalytic activity. The microscopic coexistence of the two phases means that the corrosive medium will encounter an inert FCC1 phase barrier when eroding the active FCC2 phase, which may slow down the continuous expansion of corrosion and form a 'self-limiting' corrosion process. This is quite different from the mechanism of uniform corrosion of HEA composed of single phase in corrosive media.

The OER performance of Cu50-Cu80 was further tested. Fig.7a shows the LSV diagram of the sample. It can be seen that the properties of Cu50 (327 mV @ 10 mA cm^{-2}) and Cu60 (330 mV @ 10 mA cm^{-2}) alloys are still better than other samples, and the overpotential in alkaline seawater is not much different from that in alkaline electrolyte, indicating that the alloy has strong stability and corrosion resistance. The

results of the Tafel slope (Fig.7b) are also consistent with the results of the LSV curve. Cu50 and Cu60 alloys have lower Tafel slopes and have faster catalytic reaction rates. Fig.7c is the overpotential of the sample at the current densities of 10 mA cm^{-2} and 50 mA cm^{-2}, which is consistent with the LSV curve and the Tafel slope. Fig.7d is the electrochemical impedance spectrum of OER, which is an approximate semi-circular capacitive arc, indicating that the electrode/electrolyte interface is dominated by charge transfer process, the diffusion process is not obvious, and the overall impedance level is low [43]. Similarly, the multi-impedance test of Cu50 alloy was also carried out. The obtained Bode diagram is shown in Fig.7e. As the potential increases, the corresponding charge transfer resistance decreases significantly, indicating that the OER kinetics is significantly accelerated at a higher overpotential. The phase angle shows a single peak [44], and the peak position moves slightly to high frequency with the increase of potential and the peak value decreases, indicating that the dominant process of interface reaction is gradually controlled by charge transfer. Fig.7f is the DRT spectrum of Cu50 alloy. There is only one main peak in the whole potential window, and the peak intensity decreases monotonously with the increase of overpotential [45], indicating that the charge transfer resistance Rct continues to decrease, the OER kinetics is accelerated, the interface reaction is single and the surface state is stable. Fig.7g shows the C_{dl} value of the sample. Cu50 (0.022 mF cm^{-2}) alloy has the largest C_{dl} value, which is higher than Cu60 (0.01475 mF cm^{-2}), Cu70 (0.01068 mF cm^{-2}) and Cu80 (0.00643 mF cm^{-2}) alloys, indicating that Cu50 alloy has a high electrochemical active region and plays a positive role in the catalytic effect of OER. In comparison, the Cu50 sample can exhibit

excellent OER performance and the comprehensive performance is the best. The cycle stability of Cu50 sample was analyzed (Fig.7h). After 24-h cycle stability test, its stability is still good, and the catalytic performance after cycle has only a slight decline.

In order to further explore the potential application value of the prepared electrocatalyst in the overall water splitting, the sample was then tested for total water splitting and total seawater splitting. Fig.8a shows the comparison of LSV curves of Cu50 and Cu80 alloys for total water splitting test. Fig.8b is the cycle stability test curve of Cu50 alloy in 1.0 M KOH, and it still has excellent stability after 50 h cycle. The illustration in the figure is the LSV curve before and after the cycle. The performance of Cu50 alloy after cycle test decreases slightly. It may be due to the three-step reconstruction of 'oxide layer thickening-lattice shrinkage-copper dissolution / precipitation' on the surface of the alloy during the 50 h cycle test, which increases the active layer of CoOOH/NiOOH, increases the crystallinity and decreases the porosity. The tensile stress caused by lattice contraction induces microcracks and reduces step active sites [46]. A small amount of Cu (II) is redeposited into an inert Cu_2O island after high potential dissolution, blocking the atomic boundary sites, resulting in the coverage of the active sites and the degradation of the electrocatalytic performance. Fig.8c is the LSV curve of Cu50 and Cu80 alloys in alkaline seawater electrolyte, and the two curves are not much different. The cycle stability curve in alkaline seawater electrolyte (the LSV curve before and after the cycle is shown in Fig.8d) shows that the catalyst maintains strong stability in alkaline seawater electrolyte. In alkaline seawater, Cu-based HEA may have a synergistic effect with OH^-/Cl^- to form an active phase in situ.

Cl^- may be inserted into the interlayer of hydroxide to adjust the electronic structure and optimize the adsorption energy, so the LSV curve is improved after the cycle. The results show that the prepared $Cu_x(CoCrNiFe)_{100-x}$ high-entropy alloy material has excellent structural stability and fast reaction kinetics during the reaction process, which makes the material become a highly efficient, stable and promising candidate material in water splitting applications.

4. Conclusion

In this work, we successfully prepared $Cu_x(CoCrNiFe)_{100-x}$ high-entropy alloy electrode materials by vacuum melting furnace. The alloy has good mechanical properties and exhibits excellent bifunctional activity and cycle stability in alkaline electrolyte and alkaline seawater electrolyte. This can be attributed to the high-entropy alloy has its multi-component complex microstructure and rich surface chemical state, providing a large number of electrochemically active sites. This work not only confirms the regulation of Cu content on the performance of Cu_x $(CoCrNiFe)_{100-x}$ high-entropy alloy, but more importantly, the dual FCC phase structure was successfully constructed by using liquid phase separation, which is in sharp contrast to the previous design strategy of high-entropy alloy catalyst pursuing single-phase. This phase separation structure dominated by thermodynamics can create a rich phase interface and gradient composition distribution, and synergistically optimize the electronic structure and surface adsorption characteristics, which is the key to obtain high activity and high stability at the same time. The overall performance of Cu50 alloy is good. In alkaline electrolyte, the overpotential of hydrogen evolution at the current density of -10 mA

cm^{-2} is 248.3 mV, and the overpotential of oxygen evolution at the current density of 10 mA cm^{-2} is 327 mV. In the alkaline seawater electrolysis environment, due to the synergistic passivation effect of Cl stimulating other elements, the alloy can not only resist corrosion but also maintain high catalytic activity in seawater, and the OER and HER performance are improved (at the equivalent current density, HER is 234 mV, OER is 327 mV). At the same time, it has excellent cycle stability under alkaline freshwater and alkaline seawater conditions. The reasonable strategy of this study opens up a new path for the design of high-efficiency electrocatalysts, and also provides important enlightenment and feasible direction for the deepening development of non-noble metal catalytic systems.

Acknowledgment:

This work was supported by the Project of Education Department of Liaoning Province (No. LJKMZ20220959), the National Natural Science Foundation of China (No. 51971106). Science and Technology Innovation Talent Project of Liaoning Provincial Department of Education (LJ222411632049, LJ222411632081).

Conflict of Interest:

The authors declare no conflict of interest.

Supporting information:

Supporting information is available from the author.

References:

[1] R. Bashyam, P. Zelenay, A class of non-precious metal composite catalysts for fuel cells, Nature 443 (2006) 63–66.

[2] X.P. Li, C. Huang, W.K. Han, et al., Transition metal-based electrocatalysts for overall water splitting, Chin. Chem. Lett. 32 (2021) 2597–2616.

[3] H.B. Gray, Powering the planet with solar fuel, Nat. Chem. 1 (2009) 7.

[4] O.Z. Sharaf, M.F. Orhan, An overview of fuel cell technology: Fundamentals and applications, Renew. Sustain. Energy Rev. 32 (2014) 810-853.

[5] M.G. Walter, E.L. Warren, J.R. McKone, S.W. Boettcher, Q. Mi, E.A. Santori, N.S. Lewis, Solar water splitting cells, Chem. Rev. 110 (2010) 6446-6473.

[6] SAZALI N. Emerging technologies by hydrogen: A review[J]. International Journal of Hydrogen Energy, 2020, 45(38):18753-18771.

[7] X. Li, S.-L. Xu, J. Li, S.-S. Zhang, B.-Y. Zhang, R.-D. Zhao, D.-P. Zhao, F.-F. Wu, NiFe-LDH as a bifunctional electrocatalyst for efficient water and seawater electrolysis: enhanced oxygen evolution and hydrogen evolution reactions, Nanoscale Adv. 7 (2025) 5546-5560.

[8] Y.N. Yi, Y.X. Ni, J.N. Zhang, Y. Yuan, Y. Liu, L. Wang, Y.-Y. Yang, Research progress of high-entropy alloy catalysts in water electrolysis for hydrogen production and hydrogen fuel cells, Low-Carbon Chem. Chem. Eng. 53 (2024) 62–71. (in Chinese)

[9] J.W. Yeh, S.K. Chen, S.J. Lin, et al., Nanostructured high-entropy alloys with multiple principal elements: Novel alloy design concepts and outcomes, Adv. Eng. Mater. 6 (2004) 299-303.

[10] S.M. Sha, R.Y. Ge, Y. Li, et al., High-entropy catalysts for electrochemical water-electrolysis of hydrogen evolution and oxygen evolution reactions, Front. Energy. 18 (2024) 265-290.

[11] J.T. Ren, L. Chen, H.Y. Wang, et al., High-entropy alloys in electrocatalysis: From fundamentals to applications, Chem. Soc. Rev. 52 (2023) 8319-8373.

[12] Y.Q. Zhang, D.D. Wang, S.Y. Wang, High-entropy alloys for electrocatalysis: Design, characterization, and applications, Small. 18 (2021) 2104339.

[13] X. Xiong, C. You, Z. Liu, et al., Co-Doped CuO Nanoarray: An Efficient Oxygen Evolution Reaction Electrocatalyst with Enhanced Activity, ACS Sustainable Chem. Eng. 6 (2018) 2883–2887.

[14] Y. Xin, S. Li, Y. Qian, et al., High-Entropy Alloys as a Platform for Catalysis: Progress, Challenges, and Opportunities, ACS Catal. 10 (2020) 11280–11306.

[15] Q. L. Wu, M. Luo, J.H. Han, W. Peng, Y. Zhao, D. C. Chen, M. Peng. J. Liu, Frank M. F. de Groot, Y. W. Tan, Identifying Electrocatalytic Sites of the Nanoporous Copper–Ruthenium Alloy for Hydrogen Evolution Reaction in Alkaline Electrolyte, ACS Energy Letters. 5 (2020) 192-199.

[16] Nitin K. Chaudhari, Y.J. Hong, Byeongyoon Kim, Sang-Il Choi, Kwangyeol Lee, Pt-Cu Based Nanocrystals as the Promising Catalysts for Various Electrocatalytic Reactions, Journal of Materials Chemistry A. 7 (2019) 17183-17203.

[17] N. Su, M. Y. Liu, S.L. Qiu, C.Y. Hu, X.Y. Yin, L.Q. Xiao, L.X. Hou, Skeleton-

coated CoCu-Based bimetal hollow nanoprisms as High-Performance electrocatalysts for oxygen evolution reaction, Journal of Colloid and Interface Science. 629 (2023) 763-772.

[18] Sk. Riyajuddin, S. K. Tarik Aziz, Sushil Kumar, Prof. Gilbert D. Nessim, Prof. Kaushik Ghosh, 3D-Graphene Decorated with g-C_3N_4/Cu_3P Composite: A Noble Metal-free Bifunctional Electrocatalyst for Overall Water Splitting, ChemCatChem. 12 (2020) 1394-1402.

[19] G. P. Liu, B. Wang, P. H. Ding, W. X. Wei, Y. Z. Ye, L. Wang, W. S. Zhu, H. M. Li, J. X. Xi, In-situ synthesis strategy for CoM (M=Fe,Ni,Cu) bimetallic nanoparticles decorated N-doped 1D carbon nanotubes/3D porous carbon for electrocatalytic oxygen evolution reaction, Journal of Alloys and Compounds. 815 (2020) 152470.

[20] Arslan Hameed, Faiza Zulfiqar, Waheed Iqbal, Hassan Ali, Syed Shoaib Ahmad Shah, Muhammad Arif Nadeem, Electrocatalytic water oxidation on CuO–Cu_2O modulated cobalt-manganese layered double hydroxide, RSC Advances. 12 (2022) 28954-28960.

[21] H. W. Bian, R. Wang, K. Z. Zhang, H. L. Zheng, M. J. Wen, Z. M. Li, Z. H. Li, G. X. Wang, G. W. Xie, X. Liu, L. H. Jiang, Facile electrodeposition synthesis and super performance of nano-porous Ni-Fe-Cu-Co-W high entropy alloy electrocatalyst, Surface & Coatings Technology. 459 (2023) 129407.

[22] X. D. Zhu, W. Huang, L. Tan, Z. Z. Yao, X. Yang, R. Y. Song, M. X. Chen, D. Liu, J. R. Zeng, H. Zhu, S. Lan, Ultrafast synthesis of tetragonal-distorted FeCoNiCuCr high-entropy alloy nanoparticles for enhanced OER performance, Chinese Chemical Letters. 2025, 110852.

[23] S. Q. Wang, B. L. Xu, W. Y. Huo, H. C. Feng, X. F. Zhou, F. Feng, Z. H. Xie, J. K. Shang, J. Q. Jiang, Efficient FeCoNiCuPd thin-film electrocatalyst for alkaline oxygen and hydrogen evolution reactions, Appl. Catal. B: Environ. 313 (2022) 121472.

[24] Trasatti, S.; Petrii, O. A. Real surface area measurements in electrochemistry, Pure and Applied Chemistry. 63 (1991), 711-734.

[25] S.C. Zhong, J. Li, Z. Cui, et al., Phase engineering and surface reconstruction of FeNiMo alloys as high efficient electrode for oxygen evolution reaction, J. Mater. Res. Technol. 31 (2024) 4012-4018.

[26] S. Q. Wang, W. Y. Huo, F. Fang, Z. H. Xie, J. K. Shang, J. Q. Jiang, High entropy alloy/C nanoparticles derived from polymetallic MOF as promising electrocatalysts for alkaline oxygen evolution reaction, Chem. Eng. J. 429 (2022) 132410.

[27] R. Wei, K. Zhang, P. Zhao, et al., Defect-rich FeCoNiPB/$(FeCoNi)_3O_{4-x}$ high-entropy composite nanoparticles for oxygen evolution reaction: Impact of surface activation, Appl. Surf. Sci. 549 (2021) 149327.

[28] S. Q. Wang, H. X. Yan, W. Y. Huo, A. Davydok, M. Zajac, J. Stepien, H. C. Feng, Z. H. Xie, J. K. Shang, P. H. C. Camargo, J. Q. Jiang, F. Fang, Engineering multiple nano-twinned high entropy alloy electrocatalysts toward efficient water electrolysis, Appl. Catal. B: Environ. 363 (2025) 124791.

[29] L. L. Guo, J. Q. Chi, T. Cui, J. W. Zhu, Y. N. Xia, H. L. Guo, J. P. Lai, L. Wang, Phosphorus defect mediated electron redistribution to boost anion exchange membrane-based alkaline seawater electrolysis, Adv. Energy Mater. 14 (2024) 2400975.

[30] C. Plank, T. Rüther, L. Jahn, et al., A review on the distribution of relaxation times analysis: A powerful tool for process identification of electrochemical systems, J. Power Sources 594 (2024) 233845.

[31] J. Chen, E. Quattrocchi, F. Ciucci, Y. Chen, Charging processes in lithium-oxygen batteries unraveled through the lens of the distribution of relaxation times, Chem. 9 (2023) 2267-2281.

[32] G. L. Zhang, K. S. Ming, J. L. Kang, Q. Huang, Z. J. Zhang, X. R. Zheng, X. F. Bi, High entropy alloy as a highly active and stable electrocatalyst for hydrogen evolution reaction, Electrochim. Acta. 279 (2018) 19-23.

[33] W. Yuan, B. Y. Wang, H. Wu, M. W. Xiang, Q. Wang, H. Liu, Y. Zhang, H. K. Liu, S. X. Dou, A flexible 3D nitrogen-doped carbon foam@CNTs hybrid hosting TiO_2 nanoparticles as free-standing electrode for ultra-long cycling lithium-ion batterie, J. Power Sources. 379 (2018) 10-19.

[34] B. Y. Zhang, Y. N. Zhao, X. Li, H. Y. Zhou, X. X. Zhao, R. D. Zhao, F. F. Wu, Rapidly reconstructed $CuCo_2S_4$@Co–V–O–F nanocatalysts for efficient and stable overall water splitting in alkaline and seawater electrolysis, RSC Adv. 15 (2025) 19443-19455.

[35] W.Y. Huo, S.Q. Wang, F.J. Dominguez-Gutierrez, K. Ren, Ł. Kurpaska, F. Fang, S. Papanikolaou, H.S. Kim, J.Q. Jiang, High-entropy materials for electrocatalytic applications: a review of first principles modeling and simulations, Mater. Res. Lett. 11 (2023) 713-732.

[36] K. Tiwari, C.-H. Wang, B.-S. Lou, A.M. Demeku, I. Moirangthem, S. Wang, I. Rahmadtulloh, C.-J. Wang, W. Huo, J.-W. Lee, Unveiling the potential of oxygen-rich VNbMoTaWOx high-entropy catalyst for superior anode performance for sustainable vanadium redox flow batteries. J. Power Sources 654 (2025) 237826.

[37] J. Chen, Y. Ling, X. Yu, et al., Water oxidation on CrMnFeCoNi high entropy alloy: Improvement through rejuvenation and spin polarization, J. Alloys Compd. 929 (2022) 167244.

[38] S. S. Zhang, R. Y. Li, X. Li, Y. Q. Tian, R. D. Zhao, J. Xiang, F. F. Wu, D. P. Zhao, Hydrothermally synthesized $NiSe_2$ nanospheres for efficient bifunctional electrocatalysis in alkaline seawater electrolysis: High performance and stability in HER and OER, Mater. Res. Bull. 189 (2025) 113463.

[39] M. Luo, Z. Zhao, Y. Zhang, et al., PdMo bimetallene for oxygen reduction catalysis, Nature 574 (2019) 81-85.

[40] B. Chang, Y. Ren, N. Mu, S. Zuo, C. Zou, W. Zhou, H. Zhang, Dynamic redox induced localized charge accumulation accelerating proton exchange membrane electrolysis, Adv. Mater. 37 (2025) 2405447.

[41] H. R. Ren, Z. K. Zhang, S. L. Xu, K. Jia, H. Y. Zhou, R. D. Zhao, D. P. Zhao, M. G. Li, Design and fabrication of high-performance $ZnCo_2O_4$/$ZnWS_4$ composite electrode materials for advanced asymmetric supercapacitors, Ionics.31 (2025)

8511-8524.
[42] Y. W. Pan, F. C. Zhao, G. N. Ji, S. L. Xu, R. Y. Li, H. Y. Zhou, R. D. Zhao, D. P. Zhao, F. F. Wu, Electrocatalytic performance of Ni-based high-entropy alloys with unique structural features in alkaline and seawater electrolysis under -10 °C, Int. J. Hydrogen Energy 127 (2025) 147-159.
[43] Y. Xiao, C. Tian, M. Tian, A. Wu, H. Yan, C. Chen, H. Fu, Cobalt-vanadium bimetal-based nanoplates for efficient overall water splitting, Sci. China Mater. 61 (2018) 80-90.
[44] B. Y. Zhang, S. L. Xu, J. Li, H. Y. Zhou, X. Li, R.D. Zhao, F.F. Wu, D.P. Zhao, Excellent electrocatalytic performance of $CuCo_2S_4$ nanowires for high-efficiency overall water splitting in alkaline and seawater media, CrystEngComm. 27 (2025) 3700.
[45] Y. Zheng, Y. Jiao, Y. Zhu, L.H. Li, Y. Han, Y. Chen, A. Du, M. Jaroniec, S.Z. Qiao, Hydrogen evolution by a metal-free electrocatalyst, Nat. Commun. 5 (2014) 3783.
[46] R.Y. Li, S.L. Xu, Z.Q. Ai, J.G. Qi, F. F. Wu, R.D. Zhao, D.P. Zhao, Water splitting and energy storage device through hybrid structured $ZnCo_2O_4$@NiCo-LDH nanocomposite, Int. J. Hydrogen Energy 91 (2024) 867-876.

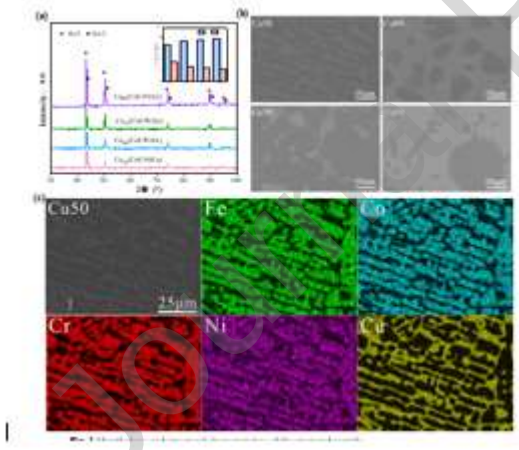

Fig. 1 Morphology and structural characteristics of the prepared sample
(a) XRD patterns (the illustration is the percentage of two phases) (b) SEM images of Cu_{50}(CoCrNiFe)- Cu_{80}(CoCrNiFe) alloys (c) Elemental mapping of Cu_{50}(CoCrNiFe) alloys

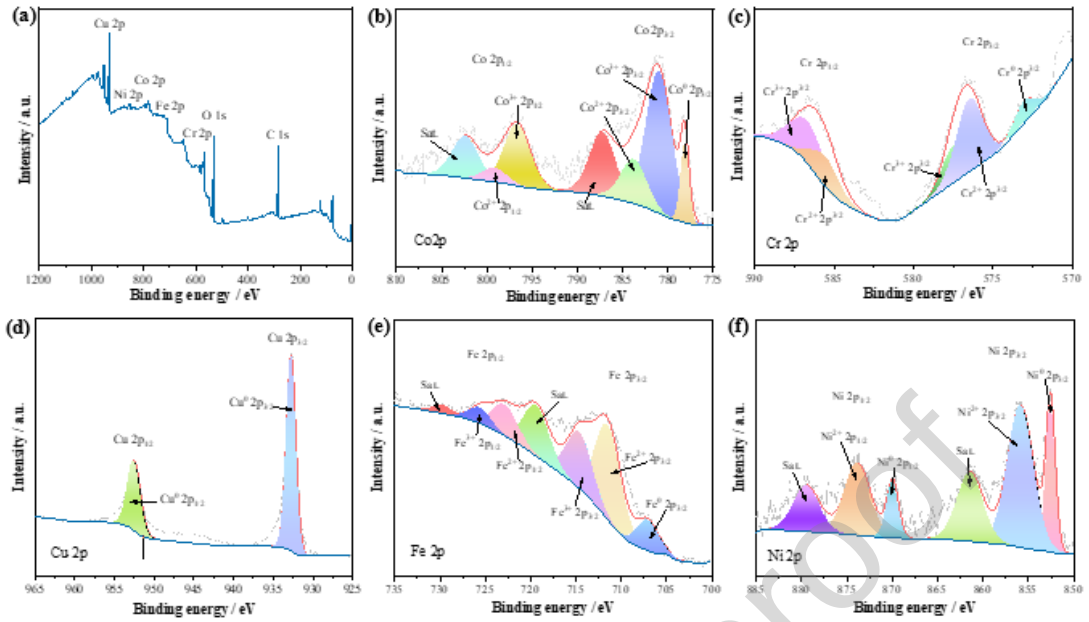

Fig. 2 Structure characterization of the as-fabricated samples (a) XPS survey (b) XPS of Co 2p (c) XPS of Cr 2p (d) XPS of Cu 2p (e) XPS of Fe 2p (f) XPS of Ni 2p

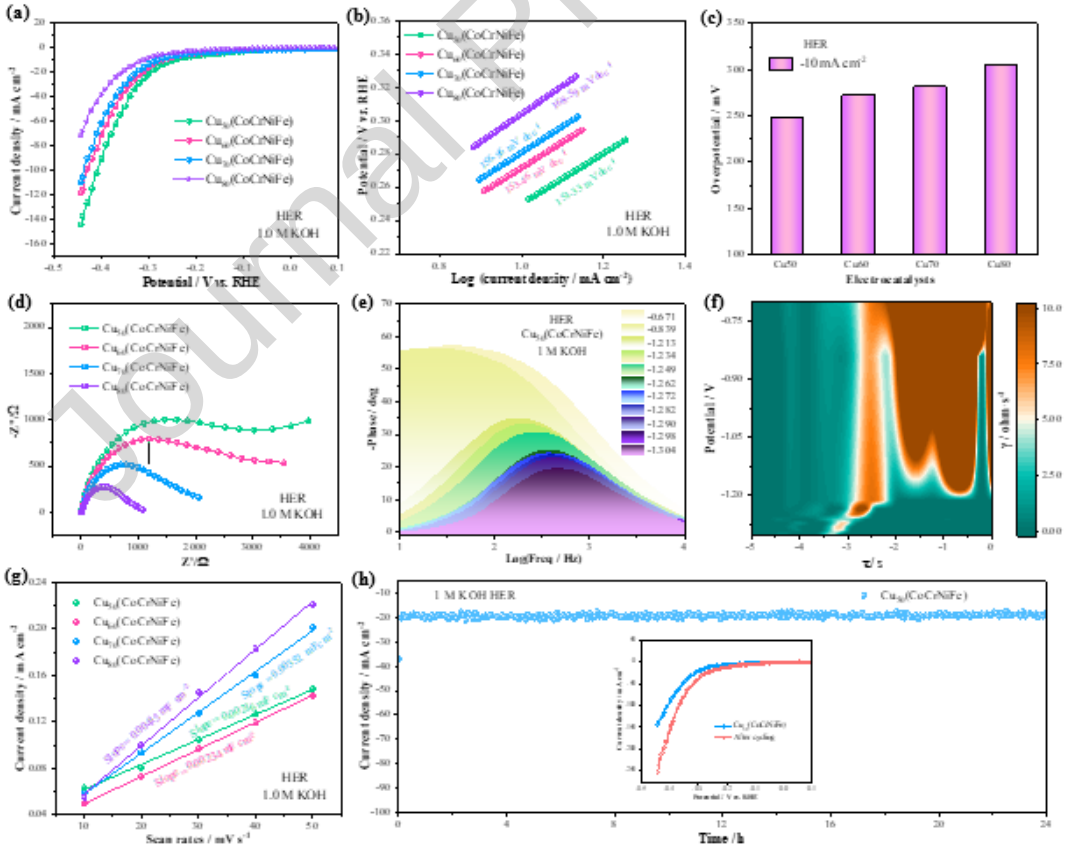

Fig. 3 Hydrogen Evolution Reaction performances in 1.0 M KOH solutions (a) Polarization curves at scan rate of 5 mV s^{-1} (b) Tafel plots (c) Overpotential at current density of -10 mA cm^{-2} (d)

Nyquist plots (e) Bode plots at multiple voltages of Hydrogen Evolution Reaction (f) DRT spectrum of Cu_{50}(CoCrNiFe) sample (g) CV curves of double-layer capacitance (C_{dl}) (h) Chronoamperometric stability tests and the insets are LSV curves

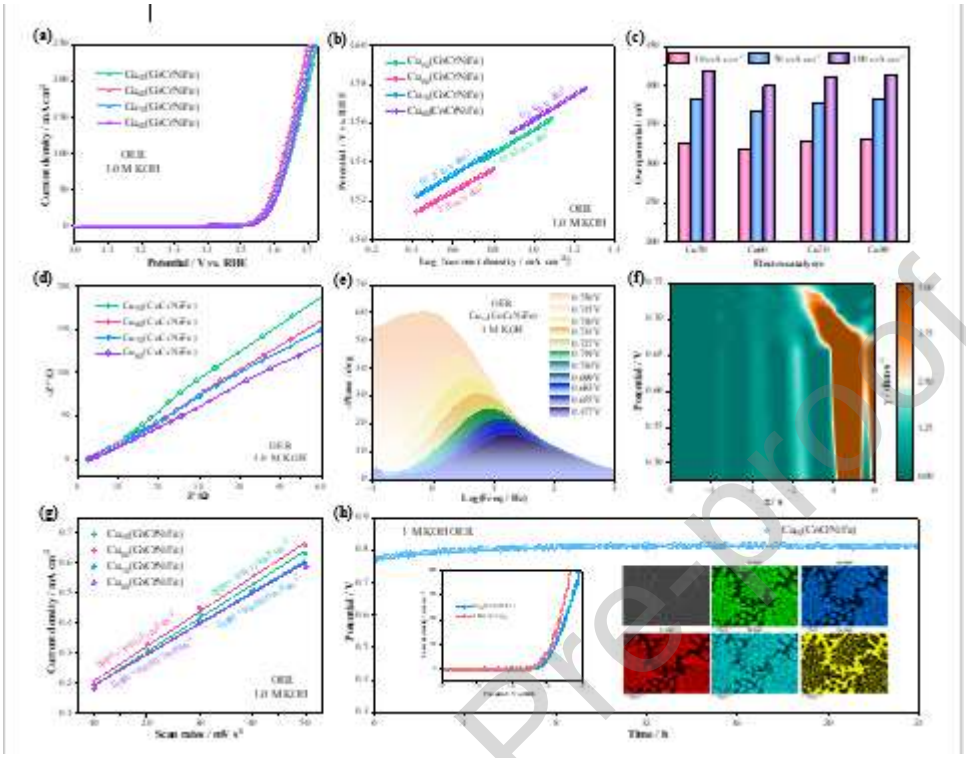

Fig. 4 Oxygen Evolution Reaction performances in 1.0 M KOH solutions (a) Polarization curves at scan rate of 5 mV s^{-1} (b) Tafel plots (c) Overpotential at the current density of 10 mA cm^{-2},50 mA cm^{-2},100 mA cm^{-2} (d) Nyquist plots (e) Bode plots at multiple voltages of Oxygen Evolution Reaction (f) DRT spectrum of Cu_{50}(CoCrNiFe) sample (g) CV curves of double-layer capacitance (C_{dl}) (h) Chronoamperometric stability tests (illustrated by LSV curve and SEM and EDS of Cu50 after cycle test)

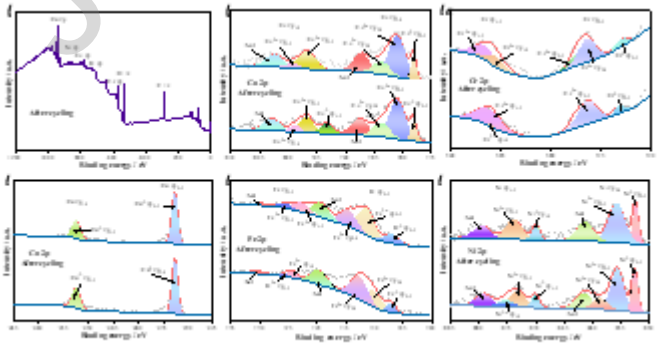

Fig. 5 Comparison of XPS images before and after cycling (a) XPS survey (b) XPS of Co 2p(c) XPS of Cr 2p (d) XPS of Cu 2p (e) XPS of Fe 2p (f) XPS of Ni 2p

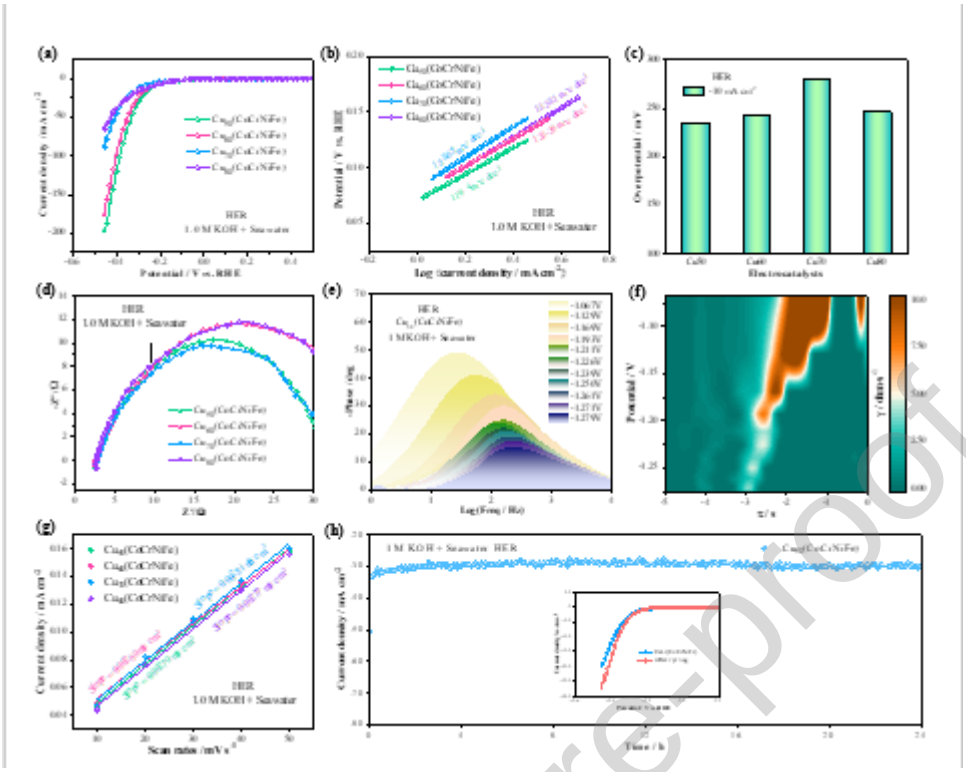

Fig. 6 Hydrogen Evolution Reaction performances of the electrocatalysts in alkaline seawater (a) Polarization curves at scan rate of 5 mV s^{-1} (b) Tafel plots (c) Overpotential at current density of -10 mA cm^{-2} (d) Nyquist plots (e) Bode plots at multiple voltages of Hydrogen Evolution Reaction (f) DRT spectrum of Cu_{50}(CoCrNiFe) sample (g) CV curves of double-layer capacitance (C_{dl}) (h) Chronoamperometric stability tests and the insets are LSV curves

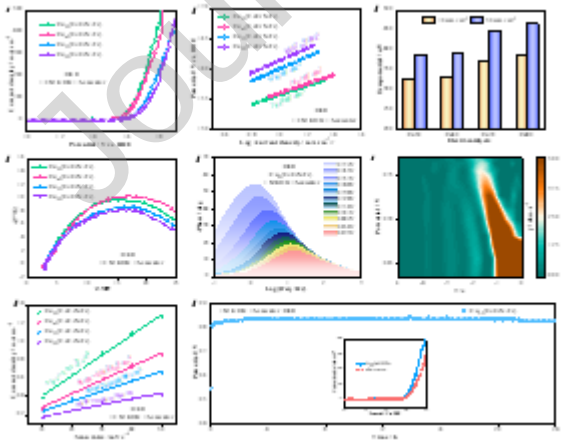

Fig. 7 Oxygen Evolution Reaction performances of the electrocatalysts in alkaline seawater (a) Polarization curves at scan rate of 5 mV s^{-1} (b) Tafel plots (c) Overpotential at the current density of 10 mA cm^{-2},50 mA cm^{-2} (d) Nyquist plots (e) Bode plots at multiple voltages of Oxygen Evolution Reaction (f) DRT spectrum of Cu_{50}(CoCrNiFe) sample (g) CV curves of double-layer capacitance (C_{dl}) (h) Chronoamperometric stability tests and the insets are LSV curves

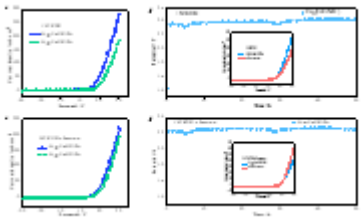

Fig. 8 overall water splitting performance of the electrocatalyst (a) LSV Curves of Cu_{50}(CoCrNiFe) and Cu_{80}(CoCrNiFe) in 1.0 M KOH (b)Chronoamperometric stability tests in 1 M KOH the inset is LSV curves before and after cycle (c) LSV Curves of Cu_{50}(CoCrNiFe) and Cu_{80}(CoCrNiFe) in alkaline seawater (d) Chronoamperometric stability tests in alkaline seawater the inset is LSV curves before and after cycle

Table 1 performance of Cu-containing electrocatalysts

Materials	HER (mV@-10 mA cm^{-2})	OER (mV@10 mA cm^{-2})	Electrolyte	Ref.
np-$Cu_{53}Ru_{47}$	~15	/	1 M KOH	[15]
Pt-Cu HBNs	20	/	1 M KOH	[16]
N-Co-Cu-S-x HNs	/	306	1 M KOH	[17]
CN/Cu_3P/3DG	67	255	1 M KOH	[18]
CoM-NCNT@PC	/	340	1 M KOH	[19]
CoMn-LDH@CuO/Cu_2O	/	297	1 M KOH	[20]
NiFeCuCoW-HEA NPs	/	247.3	1 M KOH	[21]
FeCoNiCuCr HEA NPs	/	272	1 M KOH	[22]

Declaration of Competing Interest

The data that supports the findings of this study is available from the corresponding authors upon reasonable request.